npj computational materials

www.nature.com/npjcompumats

ARTICLE OPEN

Check for updates

In-silico synthesis of lowest-pressure high-T_c ternary superhydrides

Roman Lucrezi[1], Simone Di Cataldo[1,2], Wolfgang von der Linden[1], Lilia Boeri[2,3]✉ and Christoph Heil[1]✉

We report the theoretical prediction of two high-performing hydride superconductors $BaSiH_8$ and $SrSiH_8$. They are thermodynamically stable above pressures of 130 and 174 GPa, respectively, and metastable below that. Employing anharmonic phonon calculations, we determine the minimum pressures of dynamical stability to be around 3 GPa for $BaSiH_8$ and 27 GPa for $SrSiH_8$, and using the fully anisotropic Migdal-Eliashberg theory, we predict T_c's around 71 and 126 K, respectively. We also introduce a method to estimate the lowest pressure of synthesis, based on the calculation of the enthalpy barriers protecting the $BaSiH_8$ $Fm\bar{3}m$ structure from decomposition at various pressures. This *kinetic* pressure threshold is sensibly higher than the one based on *dynamic* stability, but gives a much more rigorous limit for synthesizability.

npj Computational Materials (2022)8:119 ; https://doi.org/10.1038/s41524-022-00801-y

INTRODUCTION

The unexpected discovery of high-temperature superconductivity in high-pressure hydrides has revamped the hopes of ending the century-long quest for superconductivity at ambient conditions[1–13]. In less than five years, superhydrides have established higher and higher records for critical temperatures, starting with SH_3 (203 K)[3], LaH_{10} (265 K)[4,5], and C-S-H (288 K)[9].

While it is very exciting to strive for new superconductors with even higher T_c's attaining *hot superconductivity*[14–16], lowering the required stabilization pressures, while retaining T_c above the boiling point of nitrogen (77 K) is of even greater importance[16–22]. In fact, the discovery of a conventional (*s*-wave) superconductor with these properties would open up a wide array of technological applications in key strategical sectors such as energy conservation, climate change, and medicine. After exhausting the search space of binary hydrides, the focus of superhydride research is rapidly shifting to ternary hydrides, where the parameter space is much larger[6,17]. We have recently predicted, for example, that a ternary hydride with $LaBH_8$ composition could form an $Fm\bar{3}m$ ternary sodalite-like clathrate (SLC) structure and remain stable down to a critical pressure $p_c \sim 35$ GPa, with a $T_c = 126$ K[16,19]. Our findings were later confirmed by independent studies on the La-B-H system[21,23]. The predicted p_c of $LaBH_8$ is a factor of four lower than in binary hydrides, where p_c's are in the Megabar range, but still too high to envision any large-scale applications for this particular compound. However, through the identification of the $Fm\bar{3}m$ XYH_8 structural template, the discovery of $LaBH_8$ paved the road to the study of a whole new family of potential high-T_c ternary hydrides, where p_c and T_c may be improved even further.

In this work, using first-principles methods for crystal structure prediction and superconductivity, we identify two high-T_c alkaline-earth/silicon superhydrides, $BaSiH_8$ and $SrSiH_8$. We predict that both compounds will spontaneously form in the $Fm\bar{3}m$ XYH_8 structure at high pressures (130 and 174 GPa, respectively), and remain dynamically stable down to much lower pressures ($p_c = 3$ and 27 GPa), with superconducting T_c's of 71 and 126 K, respectively.

We also succeed in deriving a rigorous limit for the stability of $BaSiH_8$, calculating explicitly the energy barrier protecting the metastable $Fm\bar{3}m$ structure from decomposition (*kinetic* stability) as a function of pressure, using the Variable-Cell Nudged Elastic Band (VCNEB) method[24]. We find that, indeed, $Fm\bar{3}m$ $BaSiH_8$ should remain metastable at pressures well below 130 GPa. However, the *kinetic* critical pressure p_{kin} determined by the energy barrier is significantly higher (30 GPa) than the value estimated from anharmonic lattice dynamics. Similar discrepancies between dynamical and kinetic pressure of stability may explain the systematic underestimation of the predicted pressures of (meta)stability found in other high-pressure hydrides compared to experiments[11,25–27].

RESULTS

Initial screening

$BaSiH_8$ and $SrSiH_8$ were first identified through a high-throughput screening of possible substitutions of La and B by neighbouring elements into the $Fm\bar{3}m$ XYH_8 structure, as shown in Fig. 1a. In this structure – Fig. 1b – hydrogen atoms form rhombicuboctahedral cages around lanthanum; boron, being much smaller, fills the six cubic voids surrounding the cages. This structure permits a very efficient realization of a *mechanical* precompression mechanism observed in SLC binary hydrides[25,28]. To elaborate: in addition to the large central atom (La), also the smaller atom in the interstitials (B) exerts an additional pressure on the hydrogen sublattice, lowering the minimum stabilization pressure p_c[19].

We assumed that, considering different combinations of large (X) and small (Y) atoms, the superconducting properties of $LaBH_8$ could be improved even further. Aiming at identifying compounds with low critical pressures, we performed structural relaxations at 50 GPa for all combinations of X = [K, Rb, Cs, Ca, Sr, Ba, Sc, Y, and La] and Y = [B, Al, Ga, C, Si, and Ge] elements in the $Fm\bar{3}m$ XYH_8 template, and evaluated the dynamical stability of the resulting compounds by calculating the harmonic phonon dispersions on a $4 \times 4 \times 4$ grid in reciprocal space.

As shown in Supplementary Fig. 6 of the Supplementary Material (SM), the lattice constants of the relaxed structures

[1]Institute of Theoretical and Computational Physics, Graz University of Technology, NAWI Graz, 8010 Graz, Austria. [2]Dipartimento di Fisica, Sapienza Università di Roma, 00185 Rome, Italy. [3]Enrico Fermi Research Center, Via Panisperna 89 A, 00184 Rome, Italy. ✉email: lilia.boeri@uniroma1.it; christoph.heil@tugraz.at

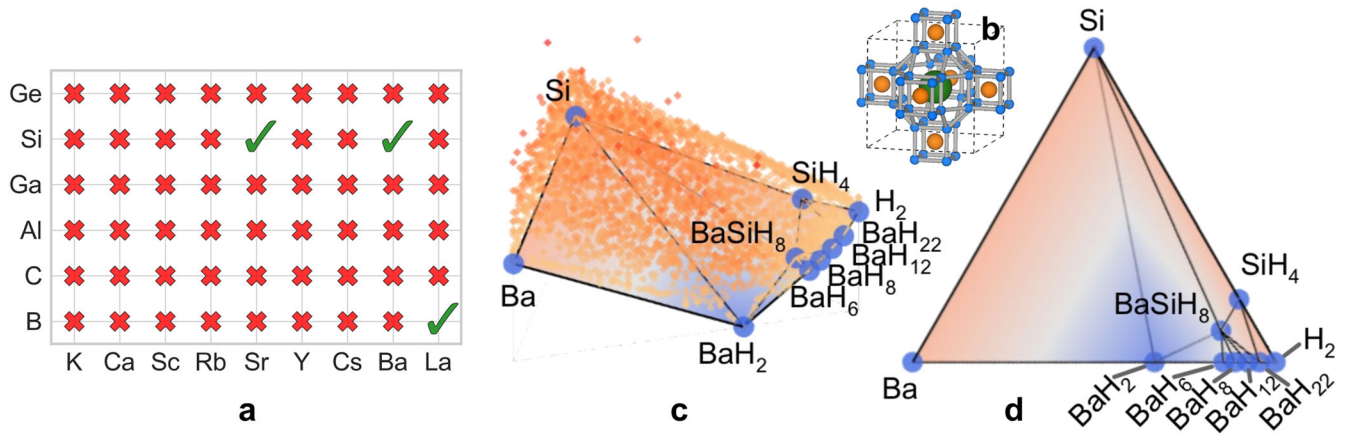

Fig. 1 Elemental composition and phase space search. a Dynamical stability of the XYH_8 structure at 50 GPa for various combinations of X and Y elements. Dynamically stable and unstable compounds are indicated by red crosses and green ticks, respectively. **b** Crystal structure of $Fm\bar{3}m$ XYH_8 in the fcc conventional unit cell; H atoms are shown in blue, H-H bonds in grey, and the lighter (heavier) atom in orange (green). **c** Ternary convex hull for $BaSiH_8$ at 100 GPa - side view; sampled structures are shown as orange dots. **d** Ternary convex hull for $BaSiH_8$ at 100 GPa - top view. In **c** and **d** the color scale (from orange to blue) represents the *depth* of the hull with respect to the elemental composition, from 0 to −0.7 eV/atom; stable compositions are shown as blue dots and are labeled.

exhibit an almost perfect linear dependence on the sum of the X and Y empirical atomic radii $R = R_X + R_Y$[29], with slopes determined by the total number of valence electrons $N_e = N_X + N_Y$. Out of the 54 compounds investigated, only three compounds with $N_e = 6$ – green ticks in Fig. 1a – are dynamically stable at 50 GPa: Apart from the already reported $LaBH_8$[19], we also found two silicon hydrides, $BaSiH_8$ and $SrSiH_8$. Both compounds exhibit a larger R than $LaBH_8$, suggesting that mechanical precompression in both compounds will be more efficient, and hence their p_c may be lower. In particular, $BaSiH_8$, where R is considerably larger than in the other two compounds, looks very promising in this respect. Indeed, our harmonic phonon calculations yield $p_c = 5$ and 30 GPa for $BaSiH_8$ and $SrSiH_8$, respectively, lower than the $p_c = 40$ GPa in $LaBH_8$.

Convex hulls and phase diagrams

Having established that $BaSiH_8$ and $SrSiH_8$ are dynamically stable in the $Fm\bar{3}m$ structure close to ambient pressure, we determined the pressures at which the two compounds may spontaneously crystallize in the $Fm\bar{3}m$ structure starting from appropriate precursors. To this end, we computed the full ternary convex hulls for the two ternary X-Si-H systems at ambient pressure and at 100 GPa, employing ab-initio variable-composition evolutionary crystal structure prediction methods as implemented in USPEX[30,31]. To construct each hull, we sampled around 20000 structures and 5000 compositions, including the contribution of the zero-point energy (ZPE) from the ionic vibrations for structures close to the hull. Our results are in good agreement with previously reported structural searches on the Ba-H and Sr-H binary hydrides[32,33]. Further computational details are given in Supplementary Method 2 and Supplementary Note 2 in the SM. An example is illustrated in Fig. 1c, d, where we show the ternary convex hull of the Ba-Si-H system at 100 GPa. (The analogous convex hull for the Sr-Si-H system at 0 and 100 GPa is shown in Supplementary Figs. 9 and 10 of the SM.)

In the Ba-Si-H system, the $BaSiH_8$ composition is thermodynamically stable, i.e., it lies on the hull at 100 GPa in a distorted $P1$ phase. The $Fm\bar{3}m$ phase is slightly higher in enthalpy (32 meV/atom), but becomes enthalpically favourable above 130 GPa. In the Sr-Si-H system at 100 GPa, according to our calculations, $SrSiH_8$ should decompose into $SrSiH_6$ and $SrSiH_{12}$, which are the stable ternary compositions along with Sr_2SiH_{10}. The corresponding structures are shown in Supplementary Fig. 12 of the SM. However, the $Fm\bar{3}m$ phase lies only 54 meV/atom above the convex hull. From a comparison of the formation enthalpies, we predict that it should become stable at 174 GPa.

Anharmonic lattice dynamics

Preliminary phonon calculations in the harmonic approximation indicated that both $BaSiH_8$ and $SrSiH_8$ experience remarkable phonon softening at lower pressures. More specifically, we find soft phonon modes, mainly at Γ (T_{2g}, E_g, and A_{1g}) and X (E_g, and additionally A_{2g} in $SrSiH_8$), as shown in Fig. 2. Eventually, imaginary frequencies appear for the E_g mode at X below 5 GPa for $BaSiH_8$ and 40 GPa for $SrSiH_8$. (A full set of phonon dispersions at all pressures considered is provided in the SM.)

Soft-mode behaviour, associated with strong anharmonicity, has been reported for many hydrogen-rich materials[25,26,34–36]. Anharmonic lattice effects have been shown to crucially affect the range of dynamical stability, phonon frequencies and eigenvectors of superhydrides, and their inclusion is essential to obtain accurate estimates of these quantities.

In order to account for anharmonic effects on the phonon dispersions of $BaSiH_8$ and $SrSiH_8$, we evaluated the adiabatic potential energy surface (APES) for every soft mode of a $2 \times 2 \times 2$ wave-vector grid, which includes explicitly the special points Γ, L, and X, and solved the resulting Schrödinger equations. (More information can be found in Supplementary Method 4 of the SM, and Ref. [37]).

The harmonic and the anharmonic phonon dispersions for $BaSiH_8$ and $SrSiH_8$ close to their critical pressures of stability are shown as dashed and full lines in Fig. 2. Anharmonicity causes a considerable hardening of the T_{2g} (at Γ) and E_g (at Γ and X) modes, leading to a decrease of the critical pressure of dynamical stability p_c: Taking this hardening into account, $SrSiH_8$ is stable down to a pressure of 27 GPa and, even more excitingly, $BaSiH_8$ down to 3 GPa.

Electronic structure and superconductivity

Having determined that both $BaSiH_8$ and $SrSiH_8$ remain dynamically stable close to ambient pressure, we are left with the question whether at these relatively low pressures they can still be considered superhydrides. A first positive indication comes from the analysis of their electronic structure.

In Fig. 3 we show the electronic dispersions and DOS for $BaSiH_8$ (left) and $SrSiH_8$ (right), at 5 and 30 GPa, respectively. Despite a scaling of the total bandwidth due to the different pressures, the band structures are qualitatively very similar. The Fermi level is

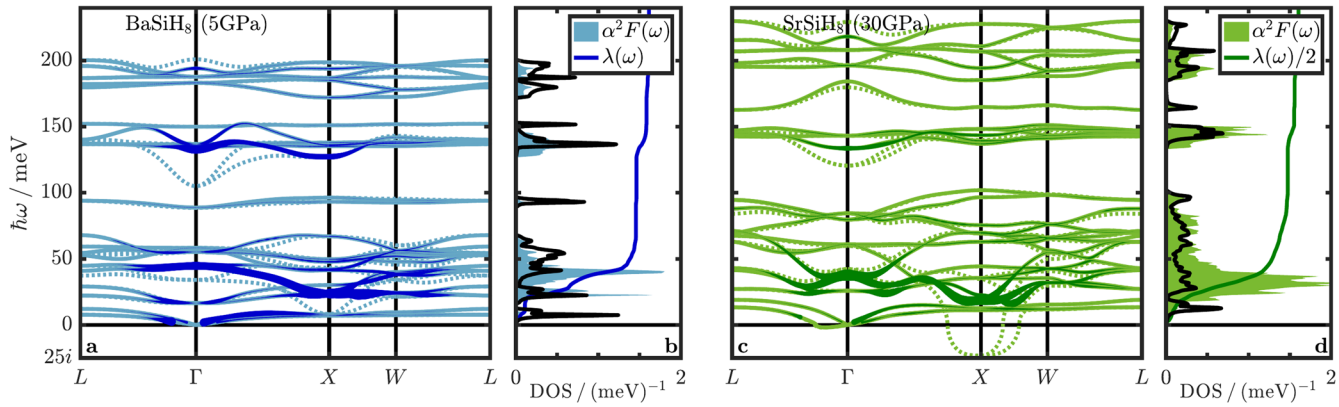

Fig. 2 Vibrational structure and electron-phonon properties. a Phonon dispersion of $BaSiH_8$ at 5 GPa; the thickness of the dark blue lines is proportional to the mode- and wave-vector resolved coupling constant $\lambda_{\mathbf{q},\nu}$. Solid (dotted) lines correspond to anharmonic (harmonic) results. **b** Phonon DOS shown as solid black line, $\alpha^2F(\omega)$ as filled curve, and $\lambda(\omega)$ as solid blue line. Panels **c** and **d** as **a** and **b** but for $SrSiH_8$ at 30 GPa.

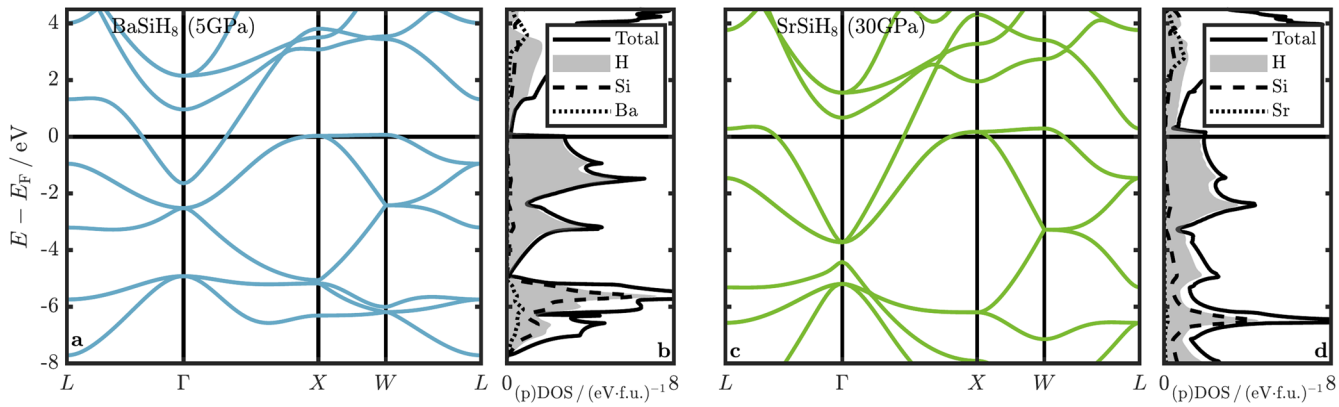

Fig. 3 Electronic band structure and density of states. a Electronic band structure of $BaSiH_8$ at 5 GPa and **b** corresponding total DOS (solid black) and projected H DOS (filled blue). Panels **c** and **d** as **a** and **b** but for $SrSiH_8$ at 30 GPa.

located just above a large DOS shoulder; in this region and up to −5.5 eV for $BaSiH_8$ (−3.5 meV for $SrSiH_8$), the bands are of purely hydrogen character. This is an important prerequisite for high-T_c conventional superconductivity in hydrides, since it can imply a strong electron-phonon (*ep*) coupling between electronic states to the light hydrogen sublattice[38].

Similar conclusions can be inferred from the electron localization function (ELF) of the two compounds (see Supplementary Fig. 15 in the SM), where, in line with what we observed in $LaBH_8$[19], we find an increased charge localization in the vicinity of the H and Si atoms and between H-H, but not between Sr/Ba and H or Si and H. This supports the idea that neither Sr/Ba, nor Si form bonds with H, and thus act on the H sublattice essentially as *mechanical* spacer, as in binary sodalite-like clathrate hydrides[6,25,34,39].

The Fermi surface topology is the same in the two compounds: a large, spheric-like electron pocket is centered around the Brillouin zone center, while a more complicated hole-like network extends around the faces of the Brillouin zone, enclosing the *X* and *W* points (see the insets of Fig. 4).

These qualitative electronic structure arguments are confirmed by actual calculations of the superconducting properties. Fig. 4 shows the energy distribution of the superconducting gap Δ as a function of temperature *T* for $BaSiH_8$ at 5 GPa pressure and for $SrSiH_8$ at 30 GPa, obtained by solving the anisotropic Migdal-Eliashberg (ME) equations on a $30\times30\times30$ **k** − and **q**-grid using the anharmonically corrected phonon dispersions with the EPW code[40,41]. (The superconducting properties at all other considered pressures and further computational details are provided in the SM.) We observe two distinct superconducting gaps: The inset of the figure shows that large Δ values correspond to the Γ-centered, spherical electron pocket, while lower values occur on the hole-like tubular network around the *X* and *W* points. The superconducting critical temperatures are predicted to be 71 and 126 K for $BaSiH_8$ and $SrSiH_8$, respectively.

Further details on the origin of the remarkable T_c's of $BaSiH_8$ and $SrSiH_8$ can be obtained from an analysis of the distribution of their *ep* coupling over phonon branches. In panel **b** of Fig. 2, the mode and wave-vector resolved *ep* coupling $\lambda_{\mathbf{q},\nu}$ are overlayed onto the phonon dispersions as fat bands; panel **d** of the same figure shows the Eliashberg spectral function $\alpha^2F(\omega)$, and the total frequency-dependent *ep* coupling parameter $\lambda(\omega)$.

The figure clearly shows that the largest contributions to the total coupling come from low-energy modes; a substantial fraction is associated to soft phonon modes around Γ and *X*. In the case of $BaSiH_8$, for example, we estimate that the phonons related to $\Gamma - T_{2g}$ contribute roughly 40% to the total λ and around $X - E_g$ about 35%. These modes are of purely hydrogen character and their patterns can be more easily visualized in terms of the H cubes around Si: The T_{2g} mode at Γ is a centrosymmetric stretching and squeezing along one of the space diagonals of the H cube, while the E_g mode at *X* is a nondeforming rotation around a face normal of the H cube, with alternating phase in two neighbouring cells.

Figure 5 shows the evolution of the superconducting properties of $BaSiH_8$ and $SrSiH_8$ as a function of pressure from the lowest dynamical stability pressure up to 100 GPa; open circles and solid lines correspond to anharmonic results, while dashed lines refer to harmonic values. Interestingly, T_c is approximately constant with pressure – panel **a**; this is true even close to p_c, where one would

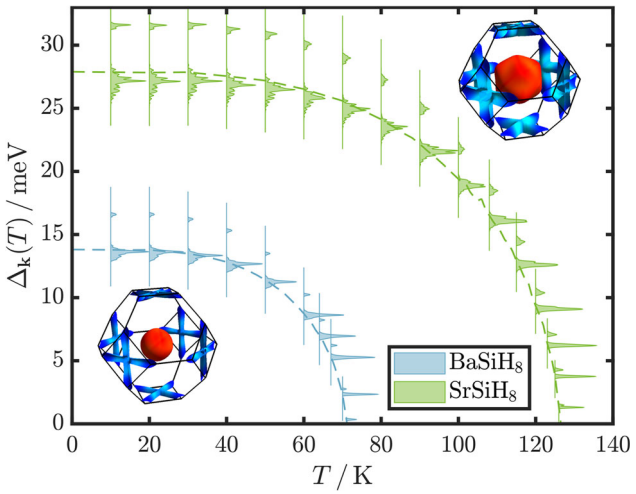

Fig. 4 Superconducting gap as a function of temperature. $\Delta(T)$ for $BaSiH_8$ (blue) at 5 GPa and for $SrSiH_8$ (green) at 30 GPa calculated using the fully anisotropic ME theory; dashed lines indicate the mean value as a guide to the eye. The insets in the top right and bottom left corner show the Fermi surface distribution of $\Delta_{\mathbf{k}}$ at 10 K for $BaSiH_8$ and $SrSiH_8$ respectively; blue/red correspond to min(Δ)/max(Δ).

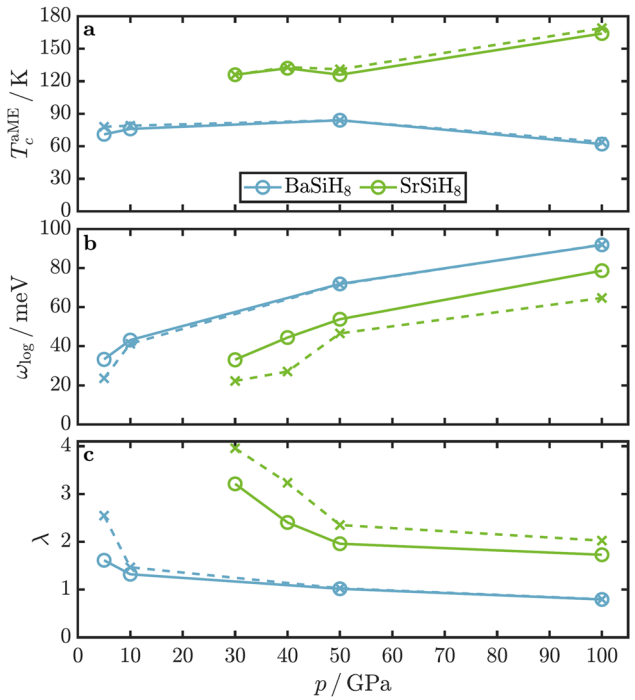

Fig. 5 Superconducting properties as a function of pressure. a T_c from anisotropic ME theory, **b** $\omega_{\log}$, and **c** λ (bottom panel) as functions of pressure for $BaSiH_8$ (blue) and $SrSiH_8$ (green). Circles and solid lines (crosses and dashed lines) indicate anharmonically corrected (harmonic) calculations. The contributions to $\alpha^2F(\omega)$ from the E_g mode at X are set to zero in the harmonic calculations for $SrSiH_8$ at 30 and 40 GPa, as the corresponding phonon frequencies are imaginary.

expect a strong deviation due to anharmonicity. An inspection of panels b and c shows that this happens because of the compensating effect of phonon hardening on $\omega_{\log}$ and λ. The effect is more marked in $SrSiH_8$ and in $BaSiH_8$ close to the instability point, where harmonic and anharmonic dispersions diverge the most. For $SrSiH_8$ at 30 GPa, we find an anharmonic (harmonic) λ of 3.21 (3.96) and an $\omega_{\log}$ of 33.1 meV (22.3 meV), and for $BaSiH_8$ at 5 GPa, we find a λ of 1.61 (2.55) and an $\omega_{\log}$ of 33.3 meV (23.7 meV).

Metastability

In all theoretical studies of high-pressure hydrides performed so far, the range of metastability of high-pressure phases has been assumed to coincide with the range of dynamical stability, eventually including quantum corrections to lattice dynamics. However, a comparison of these predictions and available experimental data suggests that theoretical estimates of the critical pressure are systematically lower than experimental values[11,25–27].

Indeed, dynamical stability is only a prerequisite for thermodynamic metastability. The latter is determined by the existence of an energy (enthalpy) barrier protecting a metastable phase from decomposition into other phases[42]. Attempts to quantitatively estimate the barrier height are extremely rare. For $Fm\bar{3}m$ $BaSiH_8$, where the dynamical instability pressure p_c is extremely close to ambient pressure, this issue is obviously crucial, since the presence of a sufficiently high barrier could be considered the definitive proof of synthesizability.

In this work, we estimated the barrier height using the VCNEB as implemented in the USPEX code[24]. In this method, a number of intermediate structures (*images*) are created between the metastable structure of interest and the ground-state structure at a given pressure; elastic forces between each image are added to the 'physical' forces, and the whole chain of images thus created is finally relaxed to obtain the energy/enthalpy profile of the transition.

We ran VCNEB simulations for $BaSiH_8$ at six different pressures: 10, 25, 35, 50, 100, and 200 GPa. As end-members for the VCNEB path, we chose the $Fm\bar{3}m$ phase and a $P1$ phase, identified as the ground-state structure at 10 GPa through a fixed-composition structural search. Due to its large unit cell and low symmetry, it can be assumed that the $P1$ phase, relaxed at the different pressures, approximates quite well the true ground-state of the system; indeed, at all pressures the $P1$ $BaSiH_8$ phase lies only a few meV above the hull. In practice, analyzing the VCNEB images in Fig. 6, we observe that the transition from the $Fm\bar{3}m$ to the $P1$ phase corresponds to the decomposition of $BaSiH_8$ into $BaSiH_6$ + H_2, with the expulsion of hydrogen in molecular form.

The potential barrier, shown in Supplementary Fig. 3, decreases with pressure from 153 meV/atom at 100 GPa to 57 meV/atom at 35 GPa; a sharp transition is visible at 25 GPa, where the kinetic barrier abruptly drops to 9 meV/atom. Although a small barrier survives down to 10 GPa, this sharp decrease is the signature of an impending *kinetic* instability, i.e., the metastable state will be short-lived and most likely will not be observed in experiments.

Combining the convex hull results in Fig. 1 with the VCNEB analysis, we can argue with confidence that an $Fm\bar{3}m$ $BaSiH_8$ phase could be synthesized above 100 GPa, and retained down to ~30 GPa, where a clearly visible enthalpy barrier exists. At lower pressures, metastable $Fm\bar{3}m$ $BaSiH_8$ will decompose, even though (anharmonic) lattice dynamics calculations predict it to be stable. Hence, *kinetic* stability poses a stricter bound for synthesizability than *dynamical* stability.

In addition to the promising theoretical synthesizability, both materials appear to be convenient in the experimental setting. As the ambient-pressure convex hulls in Figs. S7 and S9 reveal, both systems feature known stable orthorhombic binary monosilicides, namely BaSi and SrSi[43,44], which serve as adequate starting materials having the target composition of Ba/Sr and Si. The monosilicide can be loaded in a diamond anvil cell together with the common solid hydrogen storage medium ammonia borane (H_3NBH_3) which releases the hydrogen upon heating and forms the refractory compound boron nitride (BN).

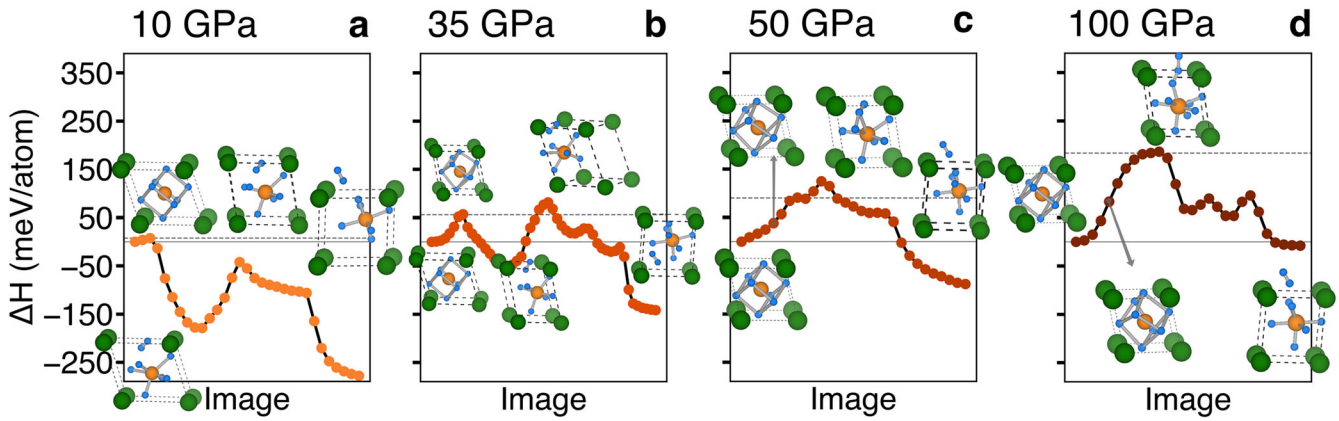

Fig. 6 VCNEB calculations for $BaSiH_8$ at different pressures. Minimum energy path (MEP) for $BaSiH_8$ at various pressures, calculated using the VCNEB method. Each point represents an individual crystal structure (image) along the path. Particularly relevant intermediate states are shown.

Discussion

In summary, our study shows that indeed the superconducting properties of the XYH_8 template can be optimized by a suitable choice of the *X* and *Y* elements. The two silicides identified in this work represent an improvement compared to $LaBH_8$: for $SrSiH_8$ we predict a dynamical stability pressure p_c of 27 GPa, with a T_c of 127 K. Using the figure of merit *S* introduced by the authors of Ref. [17], this means passing from 1.3 in H_3S and LaH_{10} to 2.2 in $LaBH_8$ to 2.7 in $SrSiH_8$. Even more remarkably, $BaSiH_8$ is predicted to be dynamically stable down to pressures of 3 GPa, with a critical temperature of 71 K, which is substantially higher than all established[45] and claimed[46] experimental T_c records for conventional superconductors at ambient pressure.

VCNEB calculations demonstrate that the shape of the potential energy landscape of $BaSiH_8$ is favorable for its synthesis in a wide range of pressures. In contrast to the binary La-B system, the Ba-Si system features also the ideal starting material for the synthesis, namely the stable monosilicide BaSi, and a possible path involves synthesis at high pressure ($p > 130$ GPa) and/or laser heating, and rapid quenching of the resulting phase to lower pressure, i.e., down to ~30 GPa, where the metastable $Fm\bar{3}m$ crystal structure is protected by a sizable potential barrier. This defines a *kinetic* threshold pressure, p_{kin}, which is substantially higher than p_c.

By defining a concrete method to estimate the synthesizability of a proposed structure, our study sets a new standard for the ab-initio design of new superconductors at high pressures, based on the more rigorous concept of *kinetic* stability, rather than dynamical stability. The existence of a distinct *kinetic* stability criterion may also be invoked to explain why many long-standing predictions of high-T_c superconductors have not been realized experimentally[47–49].

We strongly believe that the proposed method represents a major step forward towards achieving high-T_c conventional superconductivity at room pressure.

METHODS

Crystal structure prediction

Crystal structure prediction runs were carried out using evolutionary algorithms as implemented in the USPEX package[30,31,50]; the underlying total energy and structural relaxation calculations were performed using plane-waves and pseudopotentials as implemented in the Vienna ab-initio Simulation Package VASP[51]. Further computational details are provided in Supplementary Method 2 of the SM.

Electronic and vibrational properties

All density-functional theory (DFT) and density-functional perturbation theory (DFPT) calculations of electronic and vibrational properties were carried out using the plane-wave pseudopotential code QUANTUM ESPRESSO[52], scalar-relativistic optimized norm-conserving Vanderbilt pseudopotentials (ONCV)[53], and the PBE-GGA exchange and correlation functional[54]. Computational details are provided in Supplementary Method 1 of the SM.

Phase transition paths

The phase transition path between the *P*1 and $Fm\bar{3}m$-$BaSiH_8$ was evaluated using the VCNEB method as implemented in USPEX[24,30], using variable elastic constants and a variable number of images between the endpoints. The energy and forces were calculated using VASP. Further computational details are provided in Supplementary Method 3 of the SM.

Migdal-Eliashberg theory

The interpolation of the *ep* matrix elements onto dense wave-vector grids and the subsequent self-consistent solution of the fully anisotropic Migdal-Eliashberg equations were done with EPW[41]. Based on our previous work on $LaBH_8$, where we calculated the Morel-Anderson pseudopotential μ^* from first principles using *GW* and found consistent values for μ^* of about 0.1[19,25,38], we chose the same value in the current work. Further computational details are provided in Supplementary Method 5 of the SM.

Phonon anharmonicity

Anharmonic corrections to phonon frequencies were obtained by explicitly solving the Schrödinger equation for the APES of every soft mode on a $2 \times 2 \times 2$ wave-vector grid. By calculating and solving 2D APES, we also checked that phonon-phonon interactions for various modes and wave vectors can be neglected in a good first approximation. The interpolation of the real-space force constants obtained on the $2 \times 2 \times 2$ **q**-grid was performed using the corresponding harmonic support DFPT solution as implemented in the CELLCONSTRUCTOR package[55]. Further computational details are provided in Supplementary Method 4 of the SM.

DATA AVAILABILITY

The authors confirm that the data supporting the findings of this study are available within the article and its supplementary materials. Further information is available upon request.

Received: 15 December 2021; Accepted: 4 May 2022;
Published online: 25 May 2022

REFERENCES

1. Ashcroft, N. W. Metallic hydrogen: A high-temperature superconductor? *Phys. Rev. Lett.* **21**, 1748 (1968).
2. Ashcroft, N. W. Hydrogen dominant metallic alloys: High temperature superconductors? *Phys. Rev. Lett.* **92**, 187002 (2004).

3. Drozdov, A., Eremets, M., Troyan, I., Ksenofontov, V. & Shylin, S. I. Conventional superconductivity at 203 kelvin at high pressures in the sulfur hydride system. *Nature* **525**, 73 (2015).
4. Drozdov, A. et al. Superconductivity at 250 K in lanthanum hydride under high pressures. *Nature* **569**, 528 (2019).
5. Somayazulu, M. et al. Evidence for superconductivity above 260 K in lanthanum superhydride at megabar pressures. *Phys. Rev. Lett.* **122**, 027001 (2019).
6. Flores-Livas, J. A. et al. A perspective on conventional high-temperature superconductors at high pressure: Methods and materials. *Phys. Rep.* **856**, 1 (2020).
7. Sun, Y., Lv, J., Xie, Y., Liu, H. & Ma, Y. Route to a superconducting phase above room temperature in electron-doped hydride compounds under high pressure. *Phys. Rev. Lett.* **123**, 097001 (2019).
8. Semenok, D. V. et al. Superconductivity at 253 K in lanthanum–yttrium ternary hydrides. *Mater. Today* **48**, 18–28 (2021).
9. Snider, E. et al. Room-temperature superconductivity in a carbonaceous sulfur hydride. *Nature* **586**, 373 (2020).
10. Troyan, I. A. et al. Anomalous high-temperature superconductivity in YH_6. *Adv. Mater.* **33**, 2006832 (2021).
11. Kong, P. et al. Superconductivity up to 243 K in the yttrium-hydrogen system under high pressure. *Nat. Commun.* **12**, 5075 (2021).
12. Chen, W. et al. High-temperature superconducting phases in cerium superhydride with a $T_c$up to 115 K below a pressure of 1 megabar. *Phys. Rev. Lett.* **127**, 117001 (2021).
13. Boeri, L. et al. The 2021 room-temperature superconductivity roadmap. *J. Phys. Condens. Matter* **34**, 183002 (2022).
14. Peng, F. et al. Hydrogen clathrate structures in rare earth hydrides at high pressures: possible route to room-temperature superconductivity. *Phys. Rev. Lett.* **119**, 107001 (2017).
15. Grockowiak, A. et al. Hot hydride superconductivity above 550 K. *Front. Electron. Mater.* **2**, 837651 (2022).
16. Di Cataldo, S., von der Linden, W. & Boeri, L. First-principles search of hot superconductivity in La-X-H ternary hydrides. *npj Comput. Mater.* **8**, 1 (2022).
17. Pickard, C. J., Errea, I. & Eremets, M. I. Superconducting hydrides under pressure. *Annu. Rev. Condens. Matter Phys.* **11**, 57 (2020).
18. Lv, J., Sun, Y., Liu, H. & Ma, Y. Theory-orientated discovery of high-temperature superconductors in superhydrides stabilized under high pressure. *Matter Radiat. Extremes* **5**, 068101 (2020).
19. Di Cataldo, S., Heil, C., von der Linden, W. & Boeri, L. $LaBH_8$: Towards high-$T_c$low-pressure superconductivity in ternary superhydrides. *Phys. Rev. B* **104**, L020511 (2021).
20. Shipley, A. M., Hutcheon, M. J., Needs, R. J. & Pickard, C. J. High-throughput discovery of high-temperature conventional superconductors. *Phys. Rev. B* **104**, 054501 (2021).
21. Zhang, Z. et al. Design principles for high-temperature superconductors with a hydrogen-based alloy backbone at moderate pressure. *Phys. Rev. Lett.* **128**, 047001 (2022).
22. Di Cataldo, S., Von Der Linden, W. & Boeri, L. Phase diagram and superconductivity of calcium borohyrides at extreme pressures. *Phys. Rev. B* **102**, 014516 (2020).
23. Liang, X. et al. Prediction of high-$T_c$superconductivity in ternary lanthanum borohydrides. *Phys. Rev. B* **104**, 134501 (2021).
24. Qian, G.-R. et al. Variable cell nudged elastic band method for studying solid-solid structural phase transitions. *Comput. Phys. Commun.* **184**, 2111 (2013).
25. Heil, C., Di Cataldo, S., Bachelet, G. B. & Boeri, L. Superconductivity in sodalite-like yttrium hydride clathrates. *Phys. Rev. B* **99**, 220502 (2019).
26. Errea, I. et al. Quantum hydrogen-bond symmetrization in the superconducting hydrogen sulfide system. *Nature* **532**, 81 (2016).
27. Einaga, M. et al. Crystal structure of the superconducting phase of sulfur hydride. *Nat. Phys.* **12**, 835–838 (2016).
28. Liu, H., Naumov, I. I., Hoffmann, R., Ashcroft, N. & Hemley, R. J. Potential high-$T_c$superconducting lanthanum and yttrium hydrides at high pressure. *Proc. Natl Acad. Sci. U. S. A.* **114**, 6990 (2017).
29. Slater, J. Atomic radii in crystals. *J. Chem. Phys.* **41**, 3199 (1964).
30. Glass, C. W., Oganov, A. R. & Hansen, N. USPEX - evolutionary crystal structure prediction. *Comput. Phys. Commun.* **175**, 713 (2006).
31. Oganov, A. R., Lyakhov, A. O. & Valle, M. How evolutionary crystal structure prediction works-and why. *Acc. Chem. Res.* **44**, 227 (2011).
32. Chen, W. et al. Synthesis of molecular metallic barium superhydride: pseudocubic BaH_{12}. *Nat. Commun.* **12**, 273 (2021).
33. Semenok, D.V. et al. Sr-Doped Superionic Hydrogen Glass: Synthesis and Properties of SrH_{22}. *Adv. Mater.* Accepted author manuscript: 2200924 (2022)
34. Errea, I. et al. Quantum crystal structure in the 250-kelvin superconducting lanthanum hydride. *Nature* **578**, 66 (2020).
35. Borinaga, M., Errea, I., Calandra, M., Mauri, F. & Bergara, A. Anharmonic effects in atomic hydrogen: Superconductivity and lattice dynamical stability. *Phys. Rev. B* **93**, 174308 (2016).
36. Heil, C. & Boeri, L. Influence of bonding on superconductivity in high-pressure hydrides. *Phys. Rev. B* **92**, 060508 (2015).
37. Heil, C. et al. Origin of superconductivity and latent charge density wave in NbS_2. *Phys. Rev. Lett.* **119**, 087003 (2017).
38. Heil, C., Bachelet, G. B. & Boeri, L. Absence of superconductivity in iron polyhydrides at high pressures. *Phys. Rev. B* **97**, 214510 (2018).
39. Belli, F., Novoa, T., Contreras-García, J. & Errea, I. Strong correlation between electronic bonding network and critical temperature in hydrogen-based superconductors. *Nat. Commun.* **12**, 1 (2021).
40. Margine, E. R. & Giustino, F. Anisotropic Migdal-Eliashberg theory using Wannier functions. *Phys. Rev. B* **87**, 024505 (2013).
41. Poncé, S., Margine, E., Verdi, C. & Giustino, F. Epw: Electron-phonon coupling, transport and superconducting properties using maximally localized Wannier functions. *Comput. Phys. Commun.* **209**, 116 (2016).
42. Sun, W. et al. The thermodynamic scale of inorganic crystalline metastability. *Sci. Adv.* **2**, 1 (2016).
43. Pani, M. & Palenzona, A. The phase diagram of the Ba-Si system. *J. Alloy. Compd.* **454**, L1 (2008).
44. Palenzona, A. & Pani, M. The phase diagram of the Sr-Si system. *J. Alloy. Compd.* **373**, 214 (2004).
45. Nagamatsu, J., Nakagawa, N., Muranaka, T., Zenitani, Y. & Akimitsu, J. Superconductivity at 39 K in magnesium diboride. *Nature* **410**, 63 (2001).
46. Bhaumik, A., Sachan, R. & Narayan, J. High-temperature superconductivity in boron-doped q-carbon. *ACS Nano* **11**, 5351–5357 (2017).
47. Rosner, H., Kitaigorodsky, A. & Pickett, W. E. Prediction of high T_c superconductivity in hole-doped LiBC. *Phys. Rev. Lett.* **88**, 127001 (2002).
48. Savini, G., Ferrari, A. C. & Giustino, F. First-principles prediction of doped graphane as a high-temperature electron-phonon superconductor. *Phys. Rev. Lett.* **105**, 037002 (2010).
49. Saha, S., Di Cataldo, S., Amsler, M., von der Linden, W. & Boeri, L. High-temperature conventional superconductivity in the boron-carbon system: Material trends. *Phys. Rev. B* **102**, 024519 (2020).
50. Lyakhov, A. O., Oganov, A. R., Stokes, H. T. & Zhu, Q. New developments in evolutionary structure prediction algorithm USPEX. *Comput. Phys. Commun.* **184**, 1172 (2013).
51. Kresse, G. & Furthmüller, J. Efficiency of ab-initio total energy calculations for metals and semiconductors using a plane-wave basis set. *Comput. Mater. Sci.* **6**, 15 (1996).
52. Giannozzi, P. et al. Advanced capabilities for materials modelling with Quantum ESPRESSO. *J. Phys. Condens. Matter* **29**, 465901 (2017).
53. Hamann, D. R. Optimized norm-conserving Vanderbilt pseudopotentials. *Phys. Rev. B* **88**, 085117 (2013).
54. Perdew, J. P., Burke, K. & Ernzerhof, M. Generalized gradient approximation made simple. *Phys. Rev. Lett.* **77**, 3865 (1996).
55. Monacelli, L. et al. The stochastic self-consistent harmonic approximation: Calculating vibrational properties of materials with full quantum and anharmonic effects. *J. Phys. Condens. Matter* **33**, 363001 (2021).

ACKNOWLEDGEMENTS

We thank Dmitrii Semenok (Skolkovo Institute of Science and Technology) for pointing out the experimental convenience of the two proposed materials. This research was funded by the Austrian Science Fund (FWF) P 30269-N36 and P 32144-N36. For the purpose of open access, the authors have applied a CC BY public copyright license to any Author Accepted Manuscript version arising from this submission. This work was supported by the dCluster of the Graz University of Technology and the VSC-4 of the Vienna University of Technology. L.B. acknowledges support from Fondo Ateneo-Sapienza 2017-2019. S.D.C. acknowledges computational resources from CINECA, proj. IsC90-HTS-TECH_C.

AUTHOR CONTRIBUTIONS

R.L. and S.D.C. performed the calculations, and L.B. and C.H. conceived and supervised the project. All authors contributed to the discussion of the results and participated in preparing the manuscript.

COMPETING INTERESTS

The authors declare no competing interests.

ADDITIONAL INFORMATION

Supplementary information The online version contains supplementary material available at https://doi.org/10.1038/s41524-022-00801-y.

Correspondence and requests for materials should be addressed to Lilia Boeri or Christoph Heil.

Reprints and permission information is available at http://www.nature.com/reprints

Publisher's note Springer Nature remains neutral with regard to jurisdictional claims in published maps and institutional affiliations.